SPECTROSCOPY OF $^{175}LU^{+}$ FOR OPTICAL CLOCK APPLICATIONS

Eduardo Páez

(B. Eng. MSc)

A THESIS SUBMITTED

FOR THE DEGREE OF MASTER IN PHYSICS

DEPARTMENT OF PHYSICS

NATIONAL UNIVERSITY OF SINGAPORE

Supervisor: Assoc. Prof. Murray D. Barrett

Singapore November, 2016

DECLARATION

I hereby declare that this thesis is my original work and it has been written by me in its entirety. I have duly acknowledged all the sources of information which have been used in the thesis.

This thesis has also not been submitted for any degree in any university previously

Eduardo Javier Paez Barrios

Singapore November, 2016

Contents

Abstract

With the extreme precision now reached by optical clocks it is reasonable to consider redefinition of the frequency standard. In doing so, it is important to look beyond the current best-case efforts and have an eye on future possibilities. Singly ionized lutetium has recently been suggested as a potential clock candidate. Lu^+ has a particularly narrow optical transition which in combination with several advantageous properties for managing systematic uncertainties open the possibilities to implement a multi-ion crystal clock. In this work we report for the first time laser spectroscopy of the $^1S_0$ to $^3D_1$ clock transition in $^{175}Lu^+$ including important lifetimes and branching ratios relevant to clock operation

List of Figures

List of Tables

CHAPTER 1

INTRODUCTION

Nowadays, time is the physical quantity that scientist can measure with the lowest fractional systematic uncertainty. The use of optical atomic clocks to measure time and frequency represents state-of-the-art in modern precision measurement science thanks to the progress in atomic, optical and quantum science. At the same time, optical clocks have helped to advance the frontiers of science, having a strong impact on many fundamental research areas, providing improved quantum state control for quantum information/computing [**2**], deeper insights in quantum science [**3**], tighter limits on fundamental constant variation and enhanced sensitivity for tests of relativity [**4**]. Techniques developed for optical atomic clocks, such as advanced laser stabilization [**5**], coherent manipulation of atoms and novel atom trapping schemes, have given rise to new research opportunities in quantum physics.

In this chapter, the basis ideas related to atomic clocks, their importance in fundamental science and a summary of the state of the art in time and frequency measurements are provided.

1. What is a clock and what makes a clock good

At the heart of any clock is a regular oscillatory phenomenon, whether it be the swinging of a pendulum, the spring-driven oscillations of a watch, or the voltage-driven oscillations of a quartz crystal. Cycles of this local oscillator (LO) serve as a time-base on which to divide up and quantify a particular time period. A clock then, is simply an oscillator together with a mean to count periods of oscillation. How good the clock, is primarily determined by the quality of the oscillator frequency.

The quality of the oscillator is determined by how well-defined and reproducible its frequency is. Scientifically this is quantified by the stability and the accuracy: stability determines how much the measured frequency fluctuates

about its mean value, and accuracy determines how well-defined that average is. Stability is thus a measure of the precision with which we can measure a quantity associated with a measurement of the frequency and it is usually stated as a function of averaging time, since for many noise processes, the precision increases (statistical variation is reduced through averaging) with more measurements. The stability is usually set by the combination of the inherent frequency purity of the physical system (e.g., the Q-factor) and the signal-to-noise ratio with which we can measure the frequency. In contrast, the accuracy tells us how reproducible the long term average frequency is and it is normally specified by an absolute uncertainty. It is determined by systematic effects which shift the frequency away from its ideal value. Small absolute uncertainty is clearly an essential part of a good primary frequency standard. We note that in order to be able to fairly compare clocks with different oscillation frequencies, we usually express the two main clock parameters, namely, stability (or its inverse, instability, as is commonly used in clock comparisons) and the absolute uncertainty, in fractional units.

2. Atomic clocks

The basic principles of atomic clocks are rather straightforward. An oscillating electromagnetic field, be it microwave or optical, serves as a local oscillator (LO) and is referenced to the resonant frequency of a carefully chosen atomic transition. Because all atoms of a specific element are identical, they should produce the exact same frequency reference. A clock referenced to an atomic transition would therefore be far more accurate than all previous clocks.

The key point, of course, is being able to measure the undisturbed resonance frequency of an atom, which is derived from its quantized energy levels. The laws of quantum mechanics dictate that the energies of a bound system, such as an atom, have certain discrete values. An electromagnetic field at a particular frequency can boost an atom from one energy level to a higher one. Or, an atom at a high energy level can drop to a lower level by emitting energy. The resonance frequency (f_0) of an atomic oscillator is the difference between the two energy levels, E_1 and E_2 , divided by Planck's constant, h:

$$f_0 = \frac{E_2 - E_1}{h}. \tag{1.1}$$

Atoms absorb or emit energy over a small frequency range surrounding f_0 , not at f_0 alone. This spread of frequencies δf is known as the resonance width, or linewidth. The ratio of the resonance frequency to the resonance width is known as the quality factor, Q, where

$$Q = \frac{f_0}{\delta f}. \tag{1.2}$$

Because their resonance frequencies are so high, atomic clocks instantly had much higher Qs than previous clocks, which meant that they had the potential to become the world's most accurate timekeepers.

In order to stabilize the LO to an atomic transition, atoms are first prepared in one of the clock states. The clock transition is then interrogated at a frequency, f, near to resonance and the fraction of atoms transferred to the other state is measured. This provides a frequency dependent signal S and the derivative dS/df provides a frequency discriminator signal, which is used to feedback and correct the oscillator frequency. Assuming no additional noise sources, statistical fluctuations δS in the measured values of S, will result in fractional frequency errors of the stabilized oscillator that fundamentally limit the achievable stability. As noted in [**6**], the fractional frequency errors from one feedback cycle is

$$\delta y_1 = \left(\frac{\delta f}{f_0}\right)_1 = \frac{\delta S}{f_0\,(dS/df)}. \tag{1.3}$$

The resulting instability is typically quantified by the Alan deviation, σ_τ [**6**]. Assuming white frequency noise, this can be expressed

$$\sigma_y(\tau) = \left(\frac{\delta f}{f_0}\right)\sqrt{\frac{1}{M}} = \frac{\delta S}{f_0\,(dS/df)}\sqrt{\frac{T_m}{\tau}}, \tag{1.4}$$

where T_m is the duration of a single measurement, $M = \tau/T_m$ is the number of successive measurements and τ is the total measurement time. We note that T_m is proportional to $1/\Delta f$ where Δf is the width of the resonance feature.

It is instructive to note that σ_τ can be written as

$$\sigma_y(\tau) = \frac{\delta S}{S_0 Q \kappa_S} \sqrt{\frac{T_m}{\tau}}, \tag{1.5}$$

where S_0 is the signal strength on resonance, $Q = f/\Delta f$ is the quality factor of the transition, and κ is a parameter on the order of unity which depends on the line shape. This form highlights the dependence on the quality factor of the transition and the signal to noise of the measurement.

As shown in [**7**], $\sigma(\tau)$ takes on a particularly simple form if the resonance is probed using Ramsey spectroscopy [**8**]. In this case we have,

$$\sigma_y(\tau) = \frac{1}{2\pi f_0 \sqrt{N T_m \tau}}, \tag{1.6}$$

where N is the number of atoms. The dependence on f_0 highlights the benefit of going to optical transitions, and the dependence on N highlights the benefit of using many atoms.

Both Eq. 1.5 and Eq 1.6 assume there is no dead time between measurements. Intuitively we can expect that dead time should somehow degrade the performance of the clock. To see this imagine the scenario in which the dead time is approximately 50% of the clock cycle time. Further suppose that the local oscillator has a fixed average frequency but oscillates so that the frequency is on average larger during interrogation but smaller during the dead time. Clearly a measurement will then result in a frequency correction to the oscillator that was not needed. We can then see that high frequency noise on the local oscillator, which is outside the bandwidth of the feedback loop, can degrade the low frequency performance. This is known as the Dick effect and can be an important limitation to the stability of optical clocks.

3. The state-of-the-art optical atomic clocks

The development of optical atomic clocks has involved two distinct physical systems: single ions trapped in an RF Paul trap [**9**], and neutral atoms confined by an optical lattice [**10**]. In case, several different species have been considered, each with their own advantages and disadvantages in terms of overall systematic

shifts and technical complexity. By now, both systems have demonstrated inaccuracies at the 10^{-18} level [**11, 12, 13**], and neutral atoms have now surpassed the stability limits of a single ion due to the advantage of using many atoms.

Arguably, single trapped ions benefit from having relatively few systematic shifts that can be extremely well characterized and controlled. Additionally, the ion can be trapped almost indefinitely with trapping times of several hours, days or even months been routinely demonstrated. Dead time during clock operation is then limited to state preparation, laser cooling and detection and this can be a very small fraction of the clock cycle time. Thus single ion clocks can more easily reach the stability limits imposed by quantum projection noise [**7**]. Nevertheless, the relatively low stability offered by a single atom is a current bottleneck to any possible improvement in clock accuracy. Indeed, current levels of inaccuracy require several days of integration time, and thus significant improvement would require weeks or even months of operation which is not practical from an application perspective.

Neutral atoms, on the other hand, benefit from the use of many atoms, which immediately provides the potential for a large improvement in clock stability. This facilitates a rapid evaluation of systematic effects, enabling these effects to be better controlled. However, neutral atoms are only weakly confined with trapping lifetimes typically measured in seconds. This limits the duty cycle of the interrogation time in a single clock cycle. For each cycle the atomic sample is lost during detection, which requires the sample to be reloaded. This introduces a significant dead time during clock operation, placing stringent constraints on the local oscillator performance relative to the single ion counterparts. Indeed, it was this limitation that initially prevented neutral atoms from realizing the significant improvements in stability made available by their superior numbers.

Ion-based clocks are limited to single atoms primarily because of micromotion shifts, which typically have a strong dependence on position. Our group is currently investigating singly ionized lutetium, Lu^+, as a potential clock candidate. As we will discuss in Chapter 2, a particular property of Lu^+ may allow micromotion shifts to be nulled by a judicious choice of operating condition

[**14, 15**]. This would open the door to the possibility of using many ions in a Coulomb crystal [**16**], removing the stability bottleneck.

4. Outline of this thesis

The work covered in this thesis presents the initial investigations needed to establish practical clock operation with Lu^+. In chapter 2 we first describe the relevant level structure for clock operation including state preparation, detection, cooling and, of course the possible clock transitions. We also give a detailed description of the most important systematic shifts for the most convenient $^1S_0$ to $^3D_1$ transition. In chapter 3 we give details on the experimental set up used for the experiments reported in chapter 4. In chapter 5, we give an account of the first observation of the clock transition for this previously unexplored candidate. This is followed by a discussion of the current status and future work to be done.

CHAPTER 2

LUTETIUM ATOMIC STRUCTURE

Lutetium (Lu) has only recently appeared in the literature as a viable clock candidate. It was discussed in [**15**], within the context of an averaging technique that would eliminate many important shifts that impede clocks involving states of angular momentum $J > 1/2$. First estimates of crucial atomic properties [**17**] stimulated the consideration of a clock based on large Coulomb crystals [**16**]. In this chapter, we describe the basic atomic structure of singularly charged lutetium relevant to practical clock operation. We also give a discussion of the most important systematic shifts for lutetium.

1. Atomic Structure.

Lutetium atoms have 71 electrons. The ground state electron configuration of the neutral atom is $[Xe]4f^{14}6s^25d^1$ and the term symbol is $^2D_{3/2}$. Lutetium has two naturally occurring isotopes, ^{175}Lu and ^{176}Lu, with nuclear spins $I = 7/2$ and $I = 7$ respectively.

Singly ionized lutetium, Lu^+, has an electronic configuration $[Xe]4f^146s^2$ which is similar to neutral Barium with an additional filled f shell. The resulting level structure is thus similar to neutral barium with a spin singlet ground state $^1S_0$ and a low-lying set of metastable $D-$manifold. The relevant levels are shown in Fig. 2.1. All of the low-lying D levels are long lived: the $^1D_2$ lifetime is dominated by an $E2$ decay to $^1S_0$ with a lifetime of ≈180 ms, the $^3D_3$ lifetime is dominated by an $M1$ decay to $^3D_2$ with a lifetime of ≈10 s, the $^3D_2$ lifetime is dominated by a spin-forbidden $E2$ decay to $^1S_0$ with a lifetime of ≈18 s, and the $^3D_1$ decays via a highly forbidden $M1$ decay to $^1S_0$ with a lifetime of ≈87 hours.

Our group primary interest at this time is in the $^1S_0$ to $^3D_1$ transition at 847.7 nm. This is primarily motivated by nearly closed $^3D_1$ to $^3P_0$ transition at 646 nm, which provides a convenient cooling and clock state detection channel.

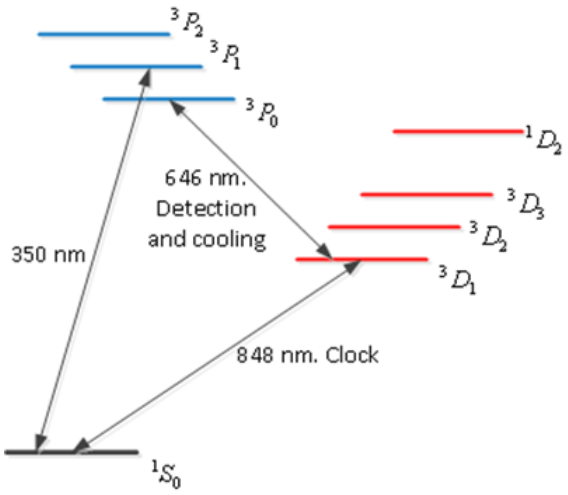

FIGURE 2.1. Lutetium 175 Electronic Structure.

We note that the extremely long lifetime of the $^3D_1$ level allows us to treat this state as an effective ground state and state detection and preparation is all done in this state. Optical pumping to this state is achieved via the $^3P_1$ level, which decays primarily to the $^1S_0$, $^3D_1$ and $^3D_2$ levels. This requires additional pump lasers to address $^1S_0$ to $^3P_1$ at 350 nm and $^3D_2$ to $^3P_1$ at 622 nm.

The $^3D_1$ to $^3P_0$ transition at 646 nm has a linewidth of 2.45 MHz. This is an order of magnitude smaller than many allowed dipole transitions for ions. As we discuss in the next section, the narrow linewidth is advantageous for Doppler cooling and the associated clock shift associated with residual thermal motion. Conversely it is sufficiently large that it provides a reasonable scattering rate to allow state-sensitive detection: experimentally we typically collect an average of 10 photons/ms. However, hyperfine mixing provides a small decay rate from $^3P_0$ to other levels predominately $^1S_0$ and $^3D_2$. This provides a fundamental limit to state detection efficiency and we experimentally characterize this in the Chapter 4.

Optical pumping through the $^3P_1$ level with both 350 nm light addressing the $^1S_0$ to $^3P_1$ transition and 622 nm light addressing the $^3D_2$ to $^3P_1$ transition facilitates pumping to the $^3D_1$ level. Conversely a 598 nm addressing $^3D_1$ to $^3P_1$ facilitates emptying of the $^3D_1$ level. In either case, occupation of the $^3P_1$ level results in a small decay rate to the inactive $^1D_2$ level, which interrupts

experiments and clock operation. We also characterize this decay channel in the Chapter 4. We note that, decay into the $^1D_2$ state is occasionally followed by decay to $^3D_3$ where the ion goes dark for periods of ≈10 s. Hence we have now invested in a laser system to clear the $^1D_2$ state to prevent this interruption.

2. Expected systematics shifts for lutetium ions.

Since this work is motivated by the $^1S_0$ to $^3D_1$ clock transition, we provide here the basic considerations of the dominant systematic shifts affecting this transition. Since the upper level has angular momentum $J = 1$, it has additional systematic shifts from rank 2 tensor interactions specifically the quadrupole and tensor polarizability shifts. The quadrupole shift in particular was the major limitation to the ultimate accuracy of the Hg^+ clock [**18**]. In the case of lutetium, these can be eliminated by averaging over multiple hyperfine state [**15**] and we start with a short summary of this technique. We then discuss the most fundamental shifts associated with any clock: the blackbody radiation (BBR) shift, the second-order Doppler shift from residual thermal motion and the second order Zeeman shift. We then discuss micromotion shifts applicable to ion-based clocks and then finally probe induced AC stark shifts which are particularly prominent for clocks with extremely long lived states as for Lu^+ and Yb^+ [**19, 4**].

2.1. Hyperfine averaging. To eliminate systematic shifts arising from additional angular momentum ($J = 1$) of the $^3D_1$ level, our group has proposed a very simple averaging technique, applicable to any level in which the nuclear spin is larger than the electronic angular momentum ($I > J$). This averaging provides an effective $J = 0$ level, [**20**].

To understand this we consider any interaction, H, which is independent of the nuclear spin. The first order energy shift for the state $|F, m_F\rangle$ is determined by the expectation value $\langle F, m_F| H |F, m_F\rangle$. By assumption, the interaction is independent of I and so it is convenient to expand the expectation value in the IJ basis. We first write,

$$|F, m_F\rangle = \sum_{m_J} C_{F,m_J} |I, J, m_F - m_J, m_J\rangle. \tag{2.1}$$

where ($\sum_F C^2_{F,m_J} = 1$). Note that, since $I > J$, this expansion includes all possible m_J states provided $|m_F| \leq I - J$. We then have,

$$\begin{aligned}\sum_F \langle F, m_F | H_Q | F, m_F \rangle & \\ &= \sum_{F,m_J,m'_J} C_{F,m_J} C_{F,m'_J} \langle J, m'_J | H_Q | J, m_J \rangle \delta_{m'_J,m_J} \\ &= \sum_{F,m_J} C^2_{F,m_J} \langle J, m_J | H_Q | J, m_J \rangle \\ &= \sum_{m_J} \langle J, m_J | H_Q | J, m_J \rangle, \end{aligned} \tag{2.2}$$

It follows that an average over F is equivalent to the average over m_J and, by the Wigner-Ekart theorem, it is equal to 0. Thus, averaging over F provides an effective $J = 0$ level in so far as many perturbations are concerns.

For Lu^+, this means that by averaging over just three transitions, we cancel quadrupole and tensor polarizability shifts and the bulk of magnetic field shifts arising from J. As with any other clocks which use averaging over multiple Zeeman states, we would not expect clock stability to be adversely affected by the averaging. We also note, that since lutetium has an even isotope with $I = 7$, $m_F = 0$ states may be used in the averaging. These are inherently insensitive to magnetic fields, so that extreme shielding is not needed for successful operation.

2.2. Second order Zeeman effect. Although hyperfine averaging cancels the dominant contributions to the Zeeman shifts arising from the dependence on J, it does not account for addition shifts arising from Zeeman mixing with other fine-structure levels. Coupling to other fine-structure levels results in a quadratic shift just as it does for other clock candidates using a $J = 0$ to $J = 0$ transition. In the case of Lu^+, the dominant contribution comes from the $^3D_2$ level and the estimated shift is given by

$$h\delta f = -\frac{\left[\mu_B B \left(g_L - g_S\right)\right]^2}{2\hbar\omega_{FS}}, \tag{2.3}$$

where $\omega_{FS} = 2\pi \times 19.16$ THz is the fine-structure splitting between the $^3D_1$ and $^3D_2$ levels. Taking $g_L \approx 1$ and $g_S \approx 2$ we find a residual quadratic shift of

just 5 Hz/mT^2. Due to the large fine structure splitting, this sensitivity is the smallest among all other clock candidates.

2.3. Black-Body Radiation. In the presence of an electric field, the energy levels of an atom experience a shift known as the Stark shift. The thermal field emitted from the atoms environment, then contributes a shift of both clock levels. Since the environment can, to a good approximation, be treated as a blackbody, this shift is referred to as the blackbody radiation shift. At practical temperatures, the thermal radiation lies in the far infrared part of the spectrum and a DC limit approximation can be used. Integrating the perturbation over the thermal distribution, the shift is given by

$$h\delta f = -\frac{1}{2}\left(831.9V/m^2\right)^2\left(\frac{T\,(K)}{T_0}\right)^4 \Delta\alpha_0\,(1+\eta)\,, \tag{2.4}$$

where $\Delta\alpha_0$ $(\alpha_e - \alpha_g)$ is the differential (DC) scalar polarizability, $T_0 = 300$K and η is a small dynamic correction. For Lu^+, an initial estimate of $\Delta\alpha_0 = -2.19$ a.u [1] [**21**], and a more recent calculation has given $\Delta\alpha_0 = 0.5$ a.u [**1**]. This gives a fraction shift at room temperature in the low 10^{-17} range. Thus temperature inaccuracies at the 1°C level should permit inaccuracies in the 10^{-18} range at room temperature. In ion traps this inaccuracy arises because the trap structure is subject to heat through the applied RF voltage, from ohmic losses in the conductors and from dielectric losses in the insulators.

2.4. Second-order Doppler shift. An atom moving in a laser field experiences a Doppler shift which to first order is linear in the velocity relative to the beam propagation direction. For a trapped atom this linear shift averages to zero leaving only a second order contribution. This second order contribution gives a fractional frequency shift

$$\frac{f - f_0}{f_0} = -\frac{E_K}{mc^2} = -\frac{\langle V^2\rangle}{2c^2}, \tag{2.5}$$

[1]Throughout we use atomic units for polarizabilities. Conversion to S.I. units is via the scale factor $4\pi\epsilon_0 a_0^3$, where a_0 is the Bohr radius.

where $\langle V^2 \rangle$ is the mean squared velocity. For a Doppler cooled atom, the velocity distribution is well described by a Maxwell-Boltzmann distribution and the fractional frequency shift is given by

$$\frac{\Delta\nu_{D2}}{\nu} = -\frac{3k_B T}{2mc^2}, \tag{2.6}$$

where T is the temperature of the atom. For a Doppler cooled atom this temperature is given by $T_D \cong \frac{\hbar\Gamma}{2k_B}$. For Lu^+ $\Gamma = 2\pi \times 2.45$ MHz and the Doppler limited fractional frequency is just 60 μK. Owing to the narrow linewidth of the $^3D_1$ to $^3P_0$ transition and the heavy mass, this is the lowest amongst all of the ion based candidates[2].

2.5. Micromotion-induced shifts. A trapped ion experiences an additional clock shift associated with the time-dependent radio-frequency (RF) field that provides the confinement. When the atom is displaced from the null position of the time-dependent, it undergoes a rapid harmonic motion at the frequency of the RF field. In addition, the electric field driving this motion causes an AC stark shift. These two effects are obvious correlated and must be considered together. Since the RF field is typically much smaller than any relevant optical frequency, the AC stark shift is described by the DC polarizability $\Delta\alpha_0$ just as for the BBR shift. As shown in [**14**], the total shift from micromotion effects can be written

$$-\left[\frac{\Delta\alpha_0}{f_0}\left(\frac{m\Omega}{Q}\right)^2 + \frac{1}{2c^2}\right]\langle {V_\mu}^2 \rangle . \tag{2.7}$$

where Ω is the RF drive frequency. When $\Delta\alpha_0 < 0$ the RF drive frequency can be chosen so that the micromotion shift vanishes independent of the micromotion amplitude as was first noted in [**17**]. With the initial estimate of $\Delta\alpha_0 = -2.19$ a.u our group has explored the possibility of an ion-based clock based on large Coulomb crystals and shown the clock operation with several hundred ions might be feasible [**16**]. This is a primary motivation for considering Lu^+ as a clock candidate. We note that, should $\Delta\alpha_0 > 0$, it will likely be

[2]Neutral atoms have readily available sub-Doppler cooling methods.

negative for the $^1S_0$-$^3D_2$ transition. Whatever the outcome is, Lu^+ will allow the possibility of a multi-ion clock to be experimentally explored.

2.6. Dynamic Stark shift. As noted in the discussion of the BBR shift, an electric field induces a Stark shift of the clock transition. This is also true for the laser field used to probe the clock transition. In this case the effect is characterized by the differential dynamic polarizability. This can be broken down into its irreducible components: the scalar part $\Delta\alpha_0$, and the tensor part α_2. Note that the tensor part only applies to the excited state since it is only non-zero for $J > 1/2$. We have also neglected the vector part which is valid provided we only use linear polarization. Assuming the transitions involved are driven with the same intensity, the tensor part vanishes under hyperfine averaging leaving only the scalar part.

The shift scales with the intensity of the probe and the probe time scales inversely with the square root of the intensity. Hence the shift becomes larger for shorter probe times. From coupling strengths, and polarizabilities given in [**1**], we estimate the fractional AC stark shift induced by the probe to be $\approx 5 \times 10^{-17}$ for a π time of 200 ms. Even fairly modest assessment of this shift should allow inaccuracies at the 10^{-18} to be reached.

CHAPTER 3

Experimental apparatus

Lasers are used throughout this work for photo-ionization, Doppler cooling, state-detection and optical pumping. We lock most lasers to transfer cavities using the PDH technique. These cavities are referenced to a laser locked to a Caesium reference cell so as to provided a well defined frequency reference.

There are two major sets of laser, those dedicated to Barium, which is used for sympathetic cooling and those dedicated to Lutetium. Details of the laser systems involved follow in the next sections. The clock laser will be explained in the chapter 5 due to its complexity and convenience in order to show the current progress in interrogating the clock transition. For completeness we also provide a brief summary of the linear Trap that was used for these experiments. A more detailed reference can be found in [**22**].

1. Laser systems

1.1. Caesium reference. Our caesium reference is a standard extended cavity diode laser (ECDL). This laser is locked to a caesium cell using saturated absorption spectroscopy as is shown in the Figure 3.1 and it is discussed in details in [**22**]. For convenience we lock the laser to the strongest transition which happens to be the transition ${}^3S_{1/2}$ $F = 4$ crossover to ${}^3P_{3/2}$ $F = 5$.

Subsequently, this laser signal splits in several paths each passing through a respective AOM, to provide fine tuning in order to ultimately reference six transfer cavities. These transfer cavities serve as references to lock the respective: Barium ionization 791 laser 1.2, Barium Doppler 493 nm and 650 nm laser 1.4, the Lutetium optical pumping 701 nm laser (then frequency doubled to get 350 nm) 1.6, the Lutetium detection/cooling 646 nm laser 1.5 and the Lutetium optical pumping 598 nm laser 1.6.

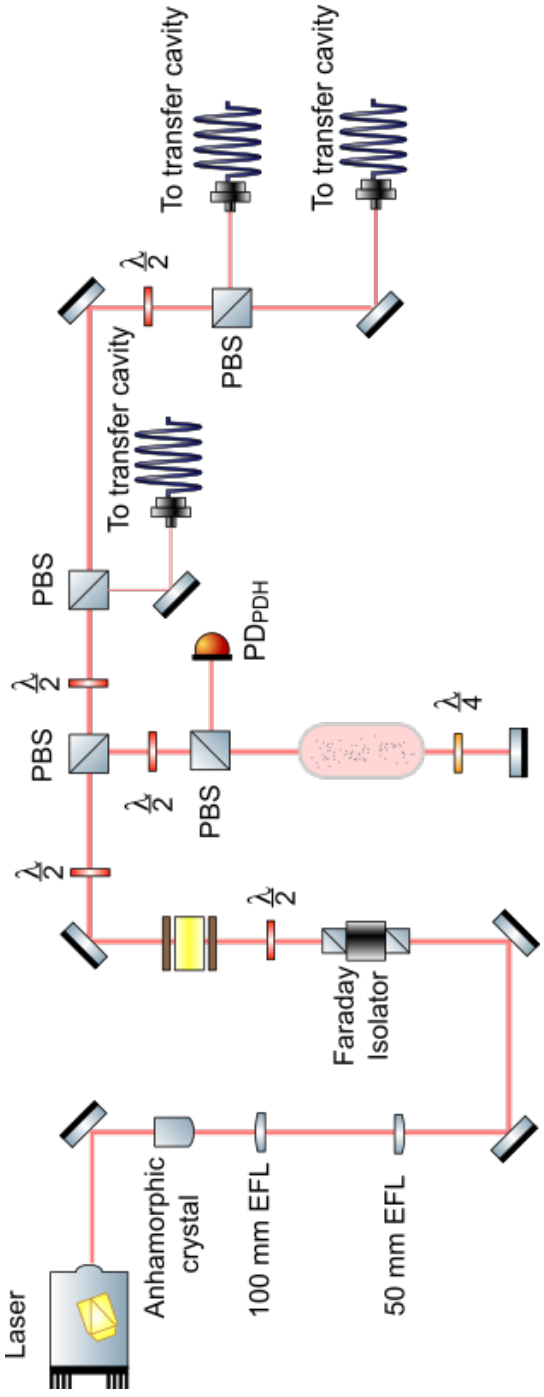

FIGURE 3.1. Optical set-up for the Caesium reference.

1.2. Barium ionizing lasers. We load Barium ions using photo-ionization. A photo-ionization technique is chosen here for two reasons. Firstly, free electrons produced in electron impact ionization tipically causes charge build-up on

insulating surfaces of the trap and it results in excess micromotion of the trapped ions which changes over time. Secondly, photo-ionization provides us isotope selectivity as the linewidth of the first excitation step is much smaller than the frequency separation between the ionizing transitions of the isotope (^{138}Ba) of interest. However, due to the geometrical configuration of the trap used, which is detailed in Section 2, there is an angle of 45° between the ionizing laser and the atom flux from the oven giving rise to Doppler broadening and shifts. To account for these Doppler effects we reduce the laser power of the first excitation process and tune the laser wavelenth appropriately as detailed in [**23**].

The ionization of ^{138}Ba is achieved via a three step excitation scheme. Briefly, the neutral barium atoms are excited from $^1S_0$ to $^3P_1$ via a 791 nm laser. Subsequently, a 450 nm laser further excites the atoms to higher lying $^3P_1$ level. From this level, any photon with a wavelength shorter than 1400 nm is able to ionize the atom. Hence, both the 791 nm and 450 nm lasers are in fact sufficient to complete the whole ionization process. However, these lasers are set to low intensity so that the isotope selectivity of the excitation process is not affected by the power broadening. This results in a low excitation rate of the third ionizing step. In [**24**] a more detailed procedure can be found. To achieve a high ionization rate, a high power 848 nm laser is sent to the trap to facilitate the final step of the ionization process. This light is conveniently provided by the clock laser.

In short, the 791 laser is locked to a transfer cavity whose reference, the Caesium signal, is shifted by an AOM in a double-pass configuration. This cavity is a confocal configuration, ceramic spacer 10 cm length, radius of curvature 10 cm and mirrors AT films 650-1100 nm. The 450 nm laser is typically in a free-running configuration and that is because this transition is broaden enough, so the need for a precise wavelength is not needed [**23**]. Both optical set-up are simple and lay out in a conventional configuration, therefore their diagrams are not shown here.

1.3. Lutetium ionizing lasers. Lutetium is also loaded in the trap using a two-photon absorption ionization at ≈452 nm laser. The first ionization step ($^2D_{3/2}$ to $^2D^o_{3/2}$) at 451.9823 nm may not provide isotope selectivity, however

the ionization threshold from this level is about 43762.39 cm^{-1} and therefore the same laser would result in easy ionization.

Due to the large hyperfine splitting of Lutetium, we can power broaden the first transitions during the ionization process to improve the loading efficiency of ^{175}Lu. This laser is set-up in a free running configuration, meanwhile the wavelength is manually set using the current and the PZT offset of the extended cavity laser around 451.98276 nm. This target corresponds to the absorption lines previously measured using a Lutetium hollow cathode lamp in an optogalvanic set-up experiment [**25**].

We lose the ability to load the isotope ^{176}Lu mainly due to Doppler broadening and its very low abundance (2.6%). This isotope is of primary interest for our goals because it has a nuclear spin $I = 7$ and therefore is inherently field insensitive providing an effective $m_F = 0$ to $m_F = 0$ transition. However, currently we have built a new ion trap with the proper geometry (Doppler free) that allows us to load efficiently ^{176}Lu.

1.4. Barium Doppler lasers. Doppler cooling is performed on the $S_{1/2}$ to $P_{1/2}$ transition, which has a transition wavelength at $\approx$ 493 nm. The $P_{1/2}$ level has a total linewidth of 20 MHz suitable for Doppler cooling, but there is a significant ($\approx$ 25%) chance of decay to the metastable $D_{3/2}$ level. This level is re-pumped using the 650 nm laser to bring the ion back to the cooling state. The electronic structure is schematically illustrated in Figure 3.2. These pair of laser are widely discussed in [**24**].

In short, the 493 laser is a commercial Toptica solution which is generated using a second harmonic generation (SHG) process using a KNbO 3 crystal placed in a bow-tie cavity (Toptica: SHG 110) for a 986 nm laser. We use the caesium signal to reference a transfer cavity allowing us to stabilize the 986 nm laser using the PDH technique by locking to the left side-band generated in an Electro-Optic modulator as indicated in Figure 3.3. This provides a large detuning as the effect for 493 nm is twice the shift of the 986 laser.

The 493 light is conveniently split in three parts each passing through a respective AOM in a double pass configuration. The first path is far detuned and high power in order to provide efficient ion loading. The second path is

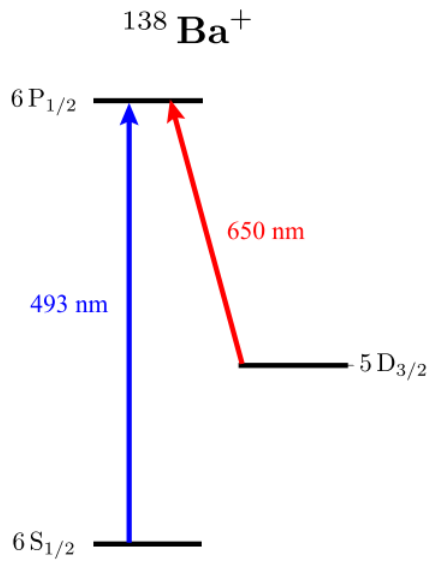

FIGURE 3.2. ^{138}Barium^{+} Electronic Structure.

used for cooling purposes while the third path is to be used for optical pumping purposes in the $S_{1/2}$ ground state. The later is exclusively used for magnetic field alignment in order to have a well defined quantization axis.

The 650 laser set-up is a standard ECDL (See Figure 3.4). It is also referenced to a transfer cavity which uses temperature tuning whose length is stabilized using the Caesium signal, the 650 light is previously shifted by an AOM in a double pass configuration. The wavelength of this laser is 649.86905 nm measured using a wavemeter of 60 MHz accuracy. This laser is also split in three paths each one goes through a double pass AOM, one with high intensity dedicated for loading ions, a second path for cooling and optical pumping and the third path is intended to be used as a tracer for optical port alignments of the trap chamber.

1.5. Lutetium detection/cooling laser. This laser is used for the cooling and state detection of Lutetium. In order to do so we have to address three hyperfine levels corresponding to the $^3D_1$ state, as a consequence we need to conveniently split this laser in order to provide the corresponding shift. The $^3D_1$ $F = 5/2, 9/2$ levels are separated 8.24 GHz and 8.36 GHz from the central hyperfine level $F = 7/2$ respectively.

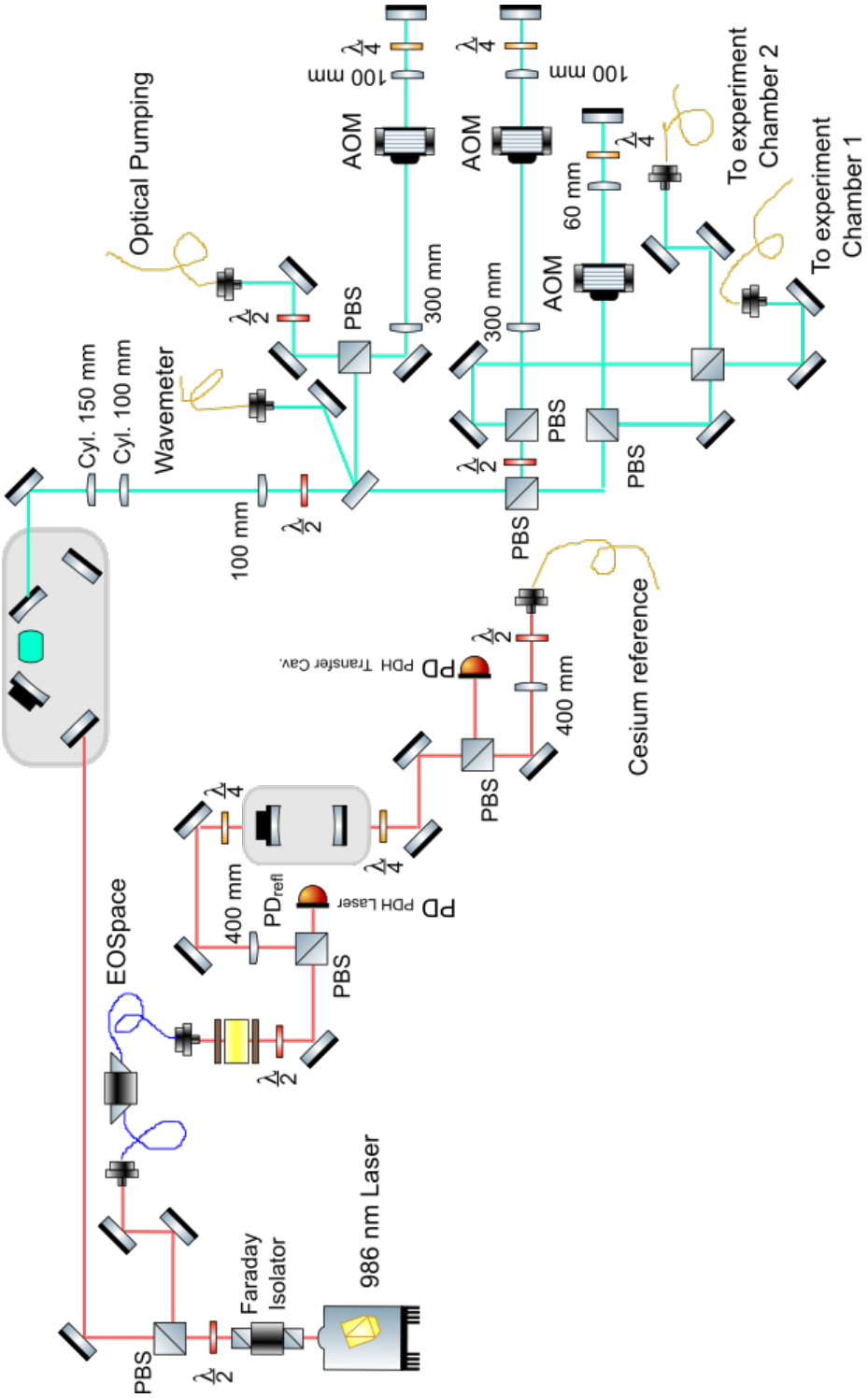

FIGURE 3.3. Diagram for 493 nm Doppler laser.

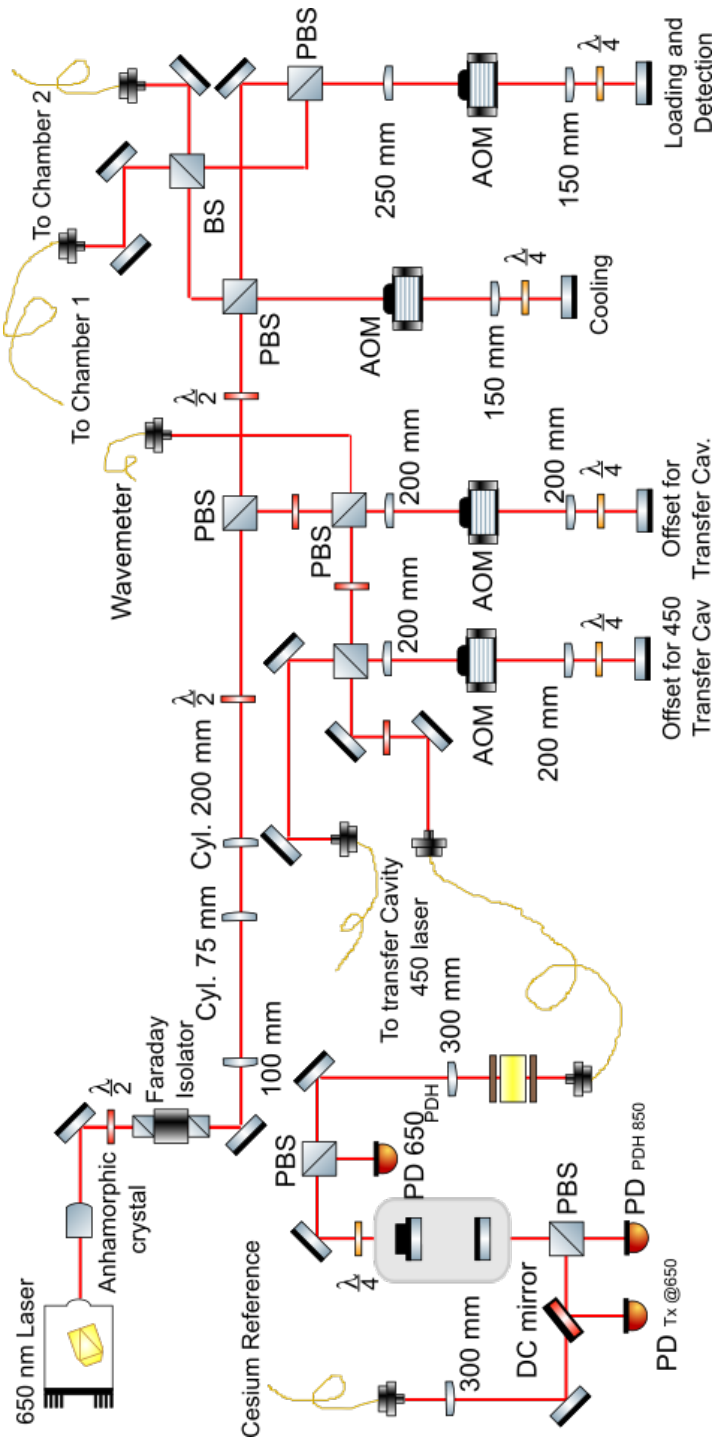

FIGURE 3.4. Diagram for 650 re-pump laser.

This laser is primarily stabilized to a transfer cavity which is fixed to the Caesium reference signal via a double-pass AOM providing fine tuning and offset

as is illustrated in the Figure 3.5. Because the hyperfine separation is near equal we can set the laser wavelength to the centre of the levels $F = 9/2$ and $F = 5/2$ and subsequently split it in two paths, one for driving the central level $F = 7/2$ shifted via AOM and the other path to drive the other two hyperfine levels using an wideband electro-optic modulator. Both paths are then recombined using a 50 : 50 beam splitter and also split in three new paths each with a proper AOM to provide optical switching and independent tuning, one path is used for cooling and state detection, the second path has high intensity light for ion loading purposes and the third one is intended to provide optical pumping in the $^3D_1$ energy level.

1.6. Lutetium optical pumping lasers. To prepare the ion in the $^3D_1$ level we clear the ground state $^1S_0$ via optical pumping into the $^3P_1$ using a 350 nm light. From this level Lutetium decays predominately to the $^3D_1$ and $^3D_2$ levels. Decay to $^3D_3$ is highly forbidden and we have not seen any evidence of direct decay to this level. Decay to $^1D_2$ occurs with a less than 1% probability, as demonstrated in Chapter 4. This branching ratio does not significantly affect experimental operation and repumping is not provided at this time. In order to provide convenient clearing of the $^3D_2$ level, we bring back the ion to $^3P_1$ by optical pumping at 622 nm. In some experimental situations it is desirable to have another optical pumping laser to clear out from the detection channel, this third laser is set at 598 nm. This set of three laser constitutes our optical pumping lasers for Lutetium. In brief, we shall review the basic operation of these lasers.

The 350 nm laser addresses the transition from $^1S_0$ F = 7/2 to $^3P_1$ F'= 7/2. This UV light is generated via SHG process of a BBO crystal placed in a bow-tie cavity as illustrated in Figure 3.6. The pump laser is a standard ECDL at 701 nm stabilized to a transfer cavity which, as in the previous cases, is referenced to the Caesium signal shifted by an AOM in a double pass configuration. Once the wavelength of the 701 laser is the desired it is locked to the transfer cavity, then this stabilized laser light is used as a reference to fix the length of the doubling cavity.

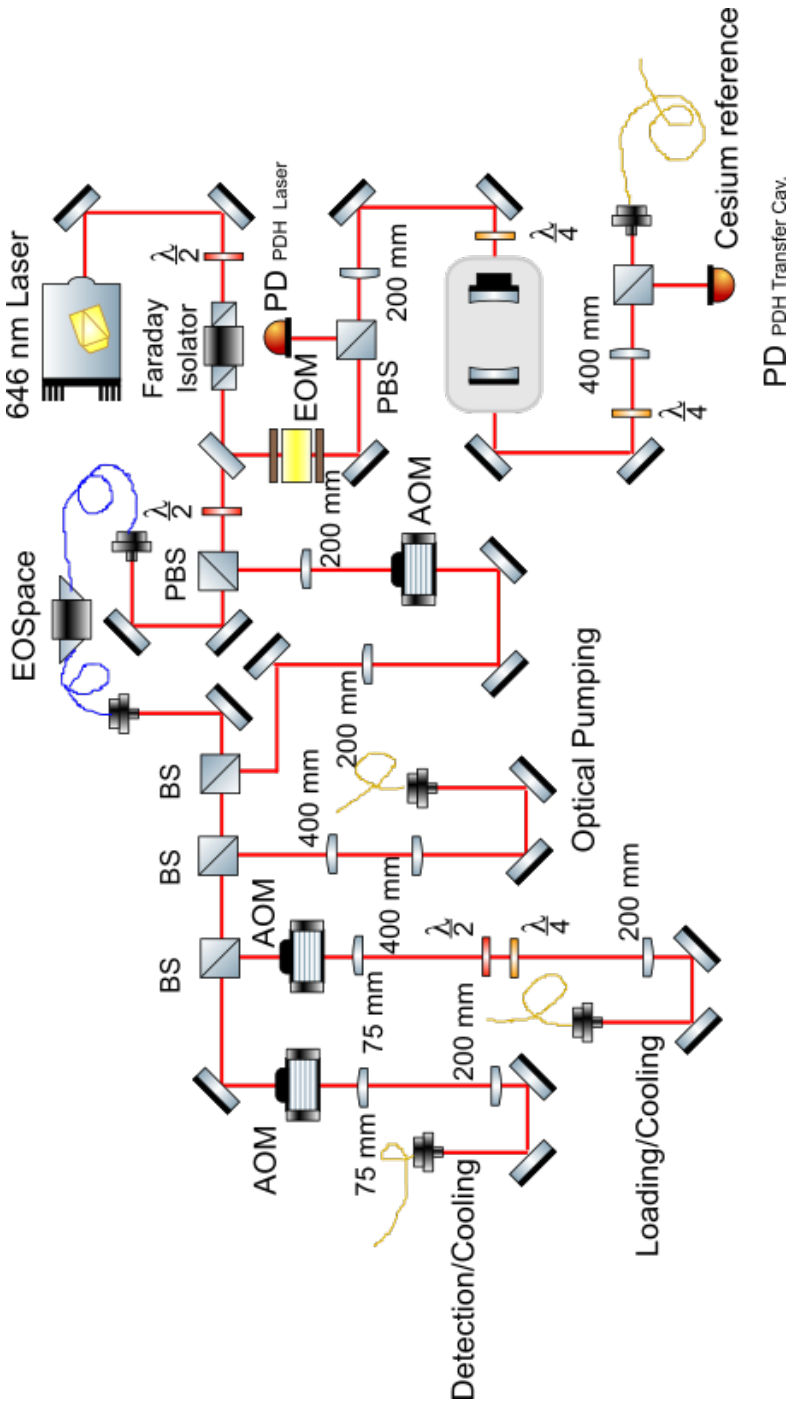

FIGURE 3.5. Diagram for 646 nm Detection/cooling laser.

The $^3D_2$ state is prevented with a multi-mode LDX-2106-622 laser part providing 150 mW in CW operation with a spectral width of ≈ 3 nm, being sufficiently broad to address all the hyperfine levels and to bring the ion back to the upper $^3P_1$.

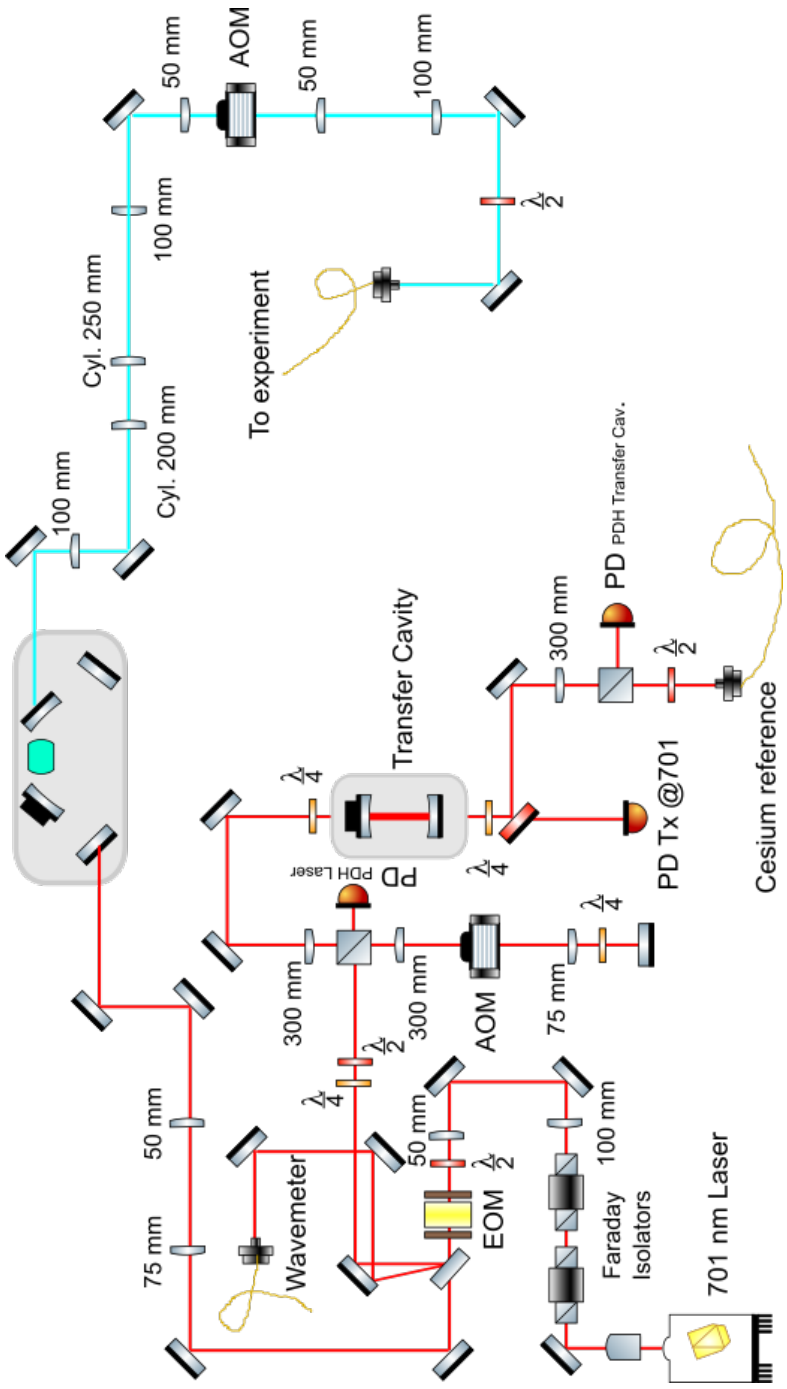

FIGURE 3.6. Diagram set-up for 350 nm doubling frequency.

The optical set-up of this laser is pretty simple. The laser is set in a free running configuration and then reshaped to provide maximum diffraction efficiency of the AOM intended for optical switching and better coupling into a

single mode fibre. Because the lifetime of this multimode diode is very short (about 2000 hours), we have recently replaced this set-up by a single mode laser at 1244 nm and light doubled using an ADVR with the corresponding set of AOM devices to provide the proper shift in order to drive all hyperfine levels.

The operation of the 598 nm optical pumping laser laser is needed to reset the state of the ion out of the detection channel. This is done, for example, when we measured the branching ratio of the $^3P_1$ level which will be detailed in the next chapter. This laser drives the transition $F = 9/2$ to $F' = 9/2$, therefore it only works efficiently when it is used in conjunction with the 646 laser when the ion is in the detection channel.

This optical set-up is slightly different of the 350 nm doubled-frequency light, see Figure 3.7 for reference. The bow-tie cavity used to generate the 598 light is stable enough to serve as an initial stabilization reference for the pump laser at 1196 nm. Once the laser is locked to this cavity, enough output light is generated at 598 for the wavemeter and also for the locking set-up to a transfer cavity. In order to find the proper wavelength for the 598 light, the length of the doubling cavity is manually changed via PZT offset. This must be done slow enough to avoid the 1196 nm laser to come unlock. Once the correct wavelength is found, the doubling cavity is locked to the transfer cavity using the caesium signal. This final step increases enough the 598 nm output light. Then, the output light is sent through a double pass AOM to provide enough detuning, optical switching and a high extinction ratio for the experiment.

2. Experiment details.

The results reported here use $^{175}Lu^+$, which has a nuclear spin $I = 7/2$. The first set of experiments designed to measure its atomic properties are performed in a four-rod linear Paul trap with axial end caps, similar to the ones described in Refs. [**26**]. The trap consists of four stainless steel rods of diameter 1.0 mm whose centres are arranged on the vertices of a square with 3.6 mm length sides.

A 3.6 MHz RF potential is applied via a step-up transformer to two diagonally opposing electrodes. A small DC voltage applied to the other two electrodes ensures a splitting of the transverse trapping frequencies. Axial confinement is

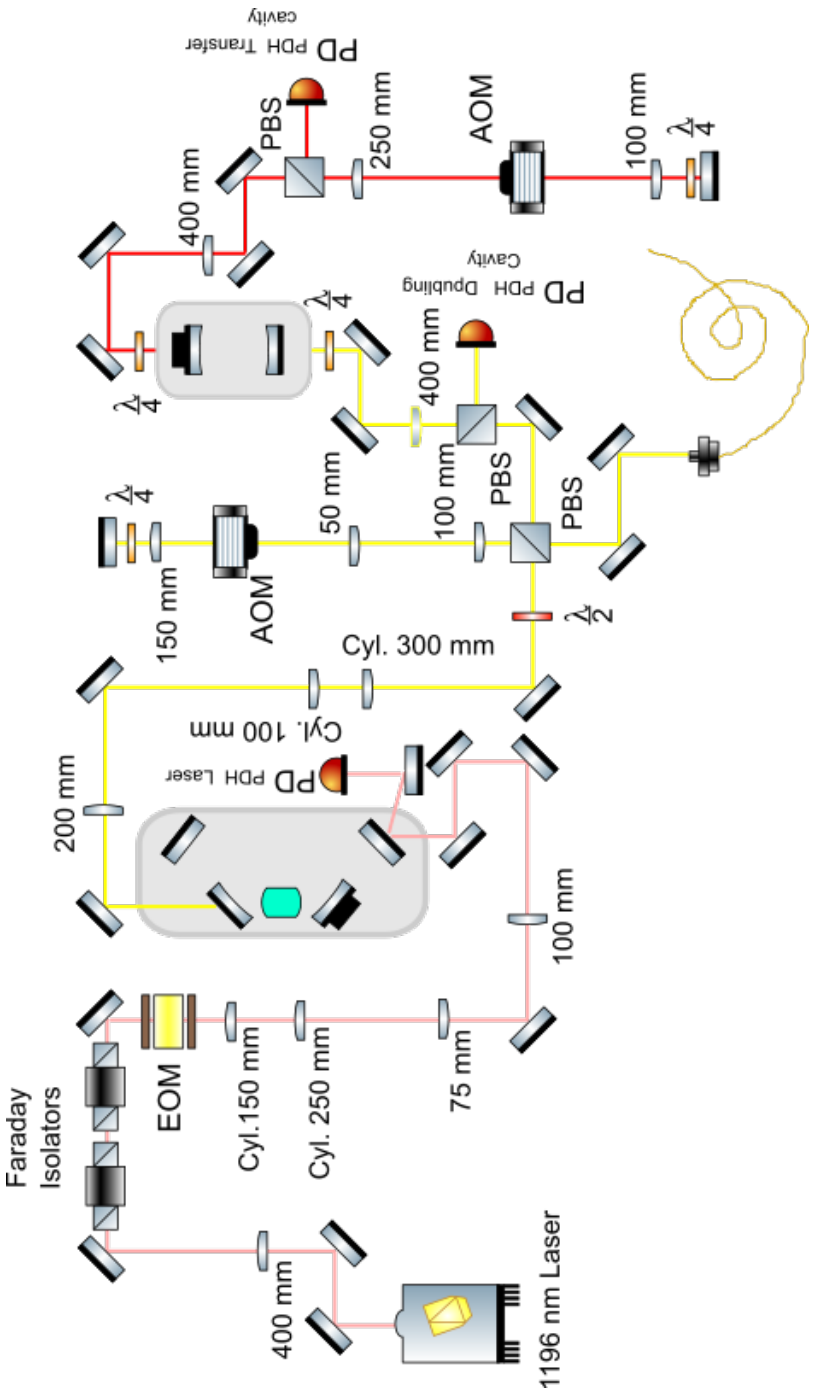

FIGURE 3.7. Optical set-up for 598 re-pump laser.

provided by two axial pins separated by 7 mm. Using this configuration, the measured trapping frequencies are $(\omega_x, \omega_y, \omega_z)/2\pi \approx (350, 300, 80)$ kHz. These frequencies were measured using $^{138}Ba^{+}$.

The imaging system used for fluorescence detection is a two-stage telescope with a total measured magnification of 7.2. After the first telescope stage a pinhole is placed in order to reduce the background level, then immediately a second stage goes straight to the CCD camera or the SPCM by using a flip mirror and a set of the proper filters. This imaging system was characterized using Barium fluorescence as will be detailed in the next chapter.

All the Barium Doppler lasers (493 and 650 lasers) are linearly polarized perpendicular to the quantization axis. This configuration avoids unwanted dark states in both the cooling and detection cycles. Additionally, the field ensures a well defined quantization axis for optical pumping and state preparation. The quantization axis is aligned using the 493 σ^+ laser propagating along the magnetic field.

Lutetium optical pumping and state preparation are achieved via the $^3P_1$ level. The 350 nm laser propagates orthogonal to a 0.5 mT $\mathbf{B}$ field and is linearly polarized along the direction of the field. The measured optical pumping time out of the $^1S_0$ level is 2 μs, which is the 1/e decay time of the $^1S_0$ population. Optical pumping out of the $^3D_1$ level is achieved in conjunction with the 598 nm and 646 nm laser and the measured optical pumping time is 6 μs. Both the 598 nm and 622 nm laser are linearly polarized and propagate along the $\mathbf{B}$ field.

CHAPTER 4

Atomic Properties of $^{175}Lu^{+}$

All of the available low-lying D states in $^{175}Lu^{+}$ are potentially long lived. These energy levels could in principle be used as clock as well. So far, we are interested in the $^{3}D_{1}$ level as a potential atomic clock, the remaining D levels could potentially complicate clock operation due to the need for a more complex laser system. On the other hand small probability decays from the $^{3}P_{1}$ level to the other D levels than the $^{3}D_{1}$, namely $^{1}D_{2}$ and $^{3}D_{2}$, implies the need of knowing precisely the lifetime of these levels and prepare the suitable lasers to optical pump appropriately.

In this chapter we give a detailed discussion of these potential issues using $^{175}Lu^{+}$. We also provide measurements of lifetimes and branching ratios relevant to practical clock operation and we make comparisons to atomic structure calculations.

1. Detection scheme

As indicated in the previous chapter, detection is achieved via scattering on the $^{3}D_{1}$ to $^{3}P_{0}$ levels. All beams are linearly polarized and propagate along the 0.5 mT magnetic field. Fluorescence at 646 nm is collected onto an avalanche photodiode (APD) with 149 Hz dark count and quantum efficiency of 55% at 650 nm. A narrowband filter eliminates scattered light from all other light sources including the 650 nm light used for cooling $^{138}Ba^{+}$. This allows continuous sympathetic cooling of $^{175}Lu^{+}$ throughout the detection window. Since the ion is continuously cooled, we can operate at near full saturation for optimum detection efficiency and we typically achieve a mean photon count rate of ≈ 5 photons/ms: 6.290(5) for bright state and 0.560(3) for dark.

For the nature of our experiments, we need a detection scheme to determine when the ion goes bright (dark) with high detection efficiency. The approach would require an FPGA to make a decision about what to do in light of several

measurements. The idea is that after a bright state is prepared the FPGA would output a TTL pulse to the counter board each time a detection window gives a bright result. This would allow LabView to be informed of the length of the bright time in units of the detection window. When the FPGA detects a dark state, it would stop sending a TTL pulse but wait to confirm the result by making more detections.

To do this we use a Bayesian detection scheme similar to that reported in [**27**]. From the number of photons collected in a given detection time step, we update the probability that the ion is in a bright state via,

$$P\left(b\left|n\right.\right)=\frac{P\left(n\left|b\right.\right)P\left(b\right)}{P\left(n\left|b\right.\right)P\left(b\right)+P\left(n\left|d\right.\right)P\left(d\right)}, \tag{4.1}$$

where $P\left(b\left|n\right.\right)$ ($P\left(d\left|n\right.\right)$) is the conditional probability the ion is in a bright (dark) state given n photons, $P\left(n\left|b\right.\right)$ ($P\left(n\left|d\right.\right)$) is the conditional probability of getting n photons given the ion is in a bright (dark) state, and $P(b)$ ($P(d)$) is the current probability the ion is in the bright (dark) state. The probability is updated in real time via a field programmable gate array with the conditional probabilities $P\left(n\left|b\right.\right)$ and $P\left(n\left|d\right.\right)$, it means, the bright and dark probability distribution for a single bin as a function of count per bin, are storage in RAM. The detection is initiated with $P(b)=0.5$ and terminated when $P(b)$ reaches pre-programmed thresholds for bright and dark states.

The FPGA used is a Nexys 4 board, ready-to-use digital circuit development platform based on the latest Artix-7 Field Programmable Gate Array (FPGA) from Xilinx.

We also require a precise measurement of the overall quantum efficiency of the system, which is determined by using the scattered light of Barium from the $P_{1/2}$ state to $D_{3/2}$ at 650 nm. That provides us a total quantum efficiency for 650 light of 0.00326(2) after repeating this procedure a few million of times.

2. $^{3}P_{1}$ Branching ratios

The $^{3}P_{1}$ decays predominantly to $^{1}S_{0}$, $^{3}D_{1}$ and $^{3}D_{2}$ with rates W_{0}, W_{1} and W_{2} respectively, also, due to spin mixing there is a very small probability of

decay to $^1D_2$ with rate W_3, of all them with branching ratios $B_k = W_k/\sum_k W_k$ and $\sum_k B_k = 1$.

We perform this measurement by first preparing the ion in the $^3D_1$ level by optically pumping with the 350, 622, and 646 nm lasers until the ion is detected bright. For this step, we set the threshold count rate to a high value to ensure the initial state is bright with high probability. At this point we make two separate experiments, we optically pump the ion into $^1S_0$ ($^3D_2$) using the 646, 598, and 622 (350) nm lasers. Then the ion is properly pumped out of the $^1S_0$ ($^3D_2$) level using the 350 (622) nm laser and the probability, P_0 (P_1), in $^3D_1$ is measured.

Neglecting any decay of population appearing in $^1D_2$ we have,

$$P_0 = \frac{B_0}{B_0 + B_3}\frac{B_1}{1 - B_0} \tag{4.2}$$

$$P_1 = \frac{B_2}{B_2 + B_3}\frac{B_1}{1 - B_2}. \tag{4.3}$$

Similarly, optical pumping to $^3D_2$, followed by optical pumping with both the 350 and 622 nm lasers, gives a population, P_2 , in the $^3D_1$ level of

$$P_2 = \frac{B_2}{B_2 + B_3}\frac{B_1}{1 - B_0 - B_2}. \tag{4.4}$$

For each P_k, 2×10^4 measurements were made giving $P_0 = 0.3027(32)$, $P_1 = 0.3166(33)$, and $P_2 = 0.9669(13)$. The inferred branching ratios from these measurements are given in Table 1 along with theoretical estimates from [**1**]. The error bars given are the statistical error. The main systematic error is due to decay of the $^1D_2$ during optical pumping. Since the measured optical pumping time for each laser is ≈ 10 μs, which is much less than the $^1D_2$ lifetime as discussed in the next section, the effect of this decay is less than the statistical error.

There is fair agreement between the experimental and theoretical results with the three main decay channels being within 4%. The larger discrepancy of $\approx$ 18% for decay to $^1D_2$ can be expected given the significantly smaller decay rate.

Lower level	Expt.	Theory
$6s^2\ ^1S_0$	0.3915(44)	0.376
$6s5d\ ^3D_1$	0.1862(17)	0.186
$6s5d\ ^3D_2$	0.4178(45)	0.435
$6s5d\ ^1D_2$	0.00438(18)	0.0036

TABLE 1. Branching ratios for decay from $^3P_1^o$. Theoretical values are from calculations given in [**1**].

3. $^1D_2$ Lifetime

The $^1D_2$ lifetime of this state is due to an $E2$ decay to $^1S_0$. However, spin mixing gives a small contribution from $M1$ transitions to $^3D_2$. The expected lifetime of this state is around 250 ms compromising in this way the evaluation of the clock transition due to an expected interrogation time of the same order of magnitude for the $^3D_1$ clock level.

To measure this lifetime we first prepare the state of the ion in the $^1S_0$ state and then keeping on for 10 ms the 350 nm, 598 nm, 622 nm and 646 nm lasers until lutetium decays into a dark state namely the $^1D_2$ level. Once dark we switch off 598 nm and wait for a bright signal by observing the 646 nm light detection channel. This analysis relies on the characterisation of pumping times. For this experiment the transfer rates into the $^3D_1$, $^3D_2$ and $^1S_0$ are on the order of a few microseconds. We should also consider possible decays to $^3D_3$ level. Those occur with a branching ratio $\approx 1\%$ and the lifetime of this state is > 10 s. Hence, these decays are infrequent and result in very long dark periods, therefore is ignored for the purpose of this experiment.

Decay to $^3D_2$ or $^1S_0$ occurs with probability q_S. These levels are optically pumped to the detection level, $^3D_1$, with a small probability, p_S, of being repumped back to $^1D_2$. Neglecting effects of decays to $^3D_3$ and optical pumping times, the distribution of dark times is exponential with a rate $W_S^{(m)} = (1 - p_S q_S)W_S$, where W_S is the total linewidth of the $^1D_2$ level. In Figure 4.1, we give the measured distribution of dark times from which we infer $W_S^{(m)} = 5.41(12)s^{-1}$. For these data we have eliminated all times less than 200 ms or greater than 1

s with 200 ms subtracted of the remaining times. Eliminating times less than 200 ms removes any data points resulting from imperfect optical pumping to the $^1D_2$ level and eliminating times greater than 1 s eliminates decays to the $^3D_3$ level.

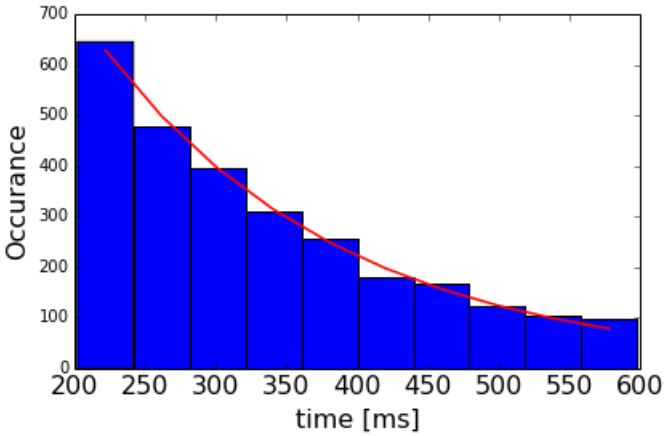

FIGURE 4.1. Histogram of dark times associated with the $^1D_2$ decay. We have omitted all times less than 200 ms or greater than 1 s with 200 ms subtracted of the remaining times.

Denoting as $W_{S,J}$ the decays to the $^1D_2$ and $^3D_2$ levels

$$W_{S,0} = \frac{W_S^{(m)} - (W_{S,1} + W_{S,3})}{1 - p_S} - W_{S,2}, \tag{4.5}$$

and

$$W_S = \frac{W_S^{(m)}}{1 - p_S} - \frac{p_S}{1 - p_S} (W_{S,1} + W_{S,3}), \tag{4.6}$$

where by definition,

$$q_S = \frac{W_{S,0} + W_{S,2}}{W_S}, \tag{4.7}$$

and p_S can be expressed in terms of the branching ratios

$$p_S = \frac{B_3}{B_1 + B_3}. \tag{4.8}$$

This may be determined from the measurements, P_k, made in section 2 and we infer $p_S = 0.02297(88)$. From the calculated $M1$ transition rates given

from [**1**] we infer decay rates 5.20(12) s^{-1} and 5.53(12) s^{-1} for $W_{S,0}$ and W_S, respectively. The errors given include only the statistical uncertainty from the experimental measurements.

4. $^3D_2$ Lifetime

We measure the $^3D_2$ lifetime similarly to the $^1D_2$ case. We first optically pump to $^3D_2$ using the 350, 598, and 646 nm lasers. After (10 ms), we switch off the 598 nm laser and monitor fluorescence of the 646 nm light. The $^3D_2$ lifetime is due to a spin-forbidden $E2$ decay to $^1S_0$ with a small contribution from an $M1$ decay to $^3D_1$. Decays to $^1S_0$ result in optical pumping to $^3D_1$ and re-pumping to $^3D_2$. Neglecting optical pumping times, the distribution of dark times is also exponential with a rate $W_T^{(m)} = (1 - p_T q_T)W_T$, where p_T is the probability of being re-pumped from $^1S_0$ to $^3D_2$ and q_T is the branching ratio for decay from $^3D_2$ to $^1S_0$. In Figure 4.2, we give the measured distribution of dark times from which we infer $W_T^{(m)} = 0.022(1)\ s^{-1}$.

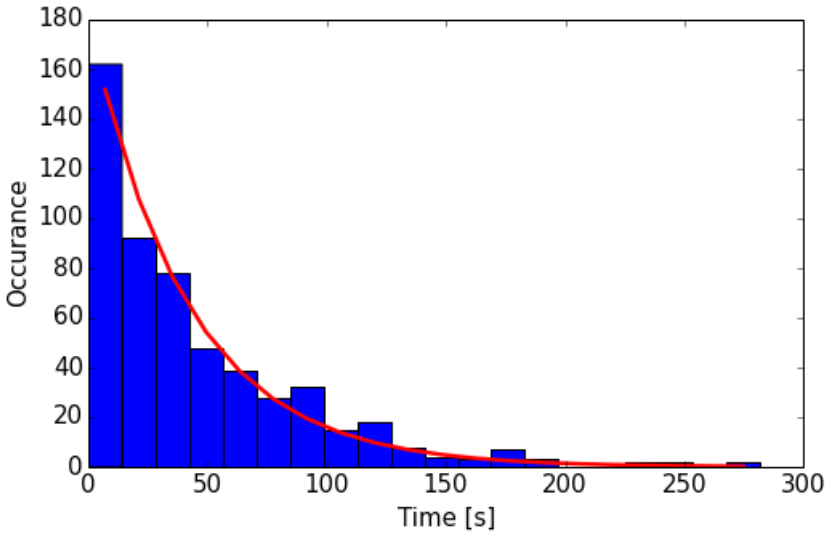

FIGURE 4.2. Histogram of dark times associated with the $^3D_2$ decay.

Note that, for each dark cycle, optically pumping to $^3P_1^o$ can result in a population of $^1D_2$ which extends the optical pumping time. Since the probability that this occurs is small and the lifetime of this state is much less than the measured mean dark time we may neglect this effect.

We can express the $E2$ decay rate, $W_{T,0}$, and total linewidth W_T as

$$W_{T,0} = \frac{1}{1-p_T}\left(W_T^{(m)} - W_{2,1}\right), \tag{4.9}$$

and

$$W_T = \frac{W_T^{(m)}}{1-p_T} - \frac{p_T}{1-p_T}W_{2,1}, \tag{4.10}$$

where $W_{2,1}$ is the $M1$ decay rate for the $^3D_2$ to $^3D_1$ transition and we have used the fact that

$$q_T = \frac{W_{T,0}}{W_T}. \tag{4.11}$$

In terms of the branching ratios, B_k, we have

$$p_T = \frac{B_2}{1-B_0}. \tag{4.12}$$

This number can be determined from the measurements, P_k, made in section 2 and we infer $p_T = 0.6917(33)$. Together with the calculated $M1$ transition rates given in [**1**] we infer decay rates 0.0519(33) and 0.0579(33) for $W_{T,0}$ and W_T, respectively. The errors given include only the statistical uncertainty from the experimental measurements.

Given that the measured lifetime is very long, measurements could potentially be compromised by off-resonant scattering out of $^3D_2$ by the barium cooling lasers (650 nm), the 350 nm re-pump laser or the 646 nm detection beam. Of these, the most significant scattering rate is from coupling to the $5d5p\ ^3F_2$ level by the 350 nm laser. From dipole matrix elements given in [**1**] and a measured intensity of ≈ 500 W/cm^2 , the scattering rate from $^3D_2$ to $^3D_1$ averaged over all possible $^3D_2$ states is $\approx 3.5 \times 10^{-5}$ s^{-1}. This less than 1% of the calculated $M1$ decay rate between these states and so contributes much less than the statistical error to the overall decay rates. We can expect scattering rates to $^3D_3$ and $^1D_2$ to be of a similar magnitude and thus equally negligible.

5. $^3P_0$ Branching ratios

Decay from $^3P_1^o$ to $^3D_1$ is the only dipole allowed transition from $^3P_0^o$. However, the hyperfine interaction induces a low multipole electromagnetic decay to other states. In the case of Lu^+, this results in a quenching of the fluorescence rate for the $^3D_1$ to $^3P_0^o$ detection channel. When fluorescing on this transition, the rate of scattering out of the detection channel is given by

$$\lambda = w\rho_{ee} = \frac{w}{W}\frac{\langle n\rangle}{q\tau_D}, \tag{4.13}$$

where W is the linewidth of the $^3P_0$ upper state, w is the total decay rate from $^3P_0^o$ to states other than $^3D_1$, $\langle n\rangle$ is the background subtracted mean number of photons collected in a time τ_D, and q is the overall detection efficiency of the imaging system. Measuring λ involves determining when the ion goes dark and so the measured rate must also include the error rate in that determination. Even an error rate of 1×10^{-3} in a 1 ms detection time would result in a significant contribution to the measured rate. Since there is negligible probability of re-pumping from the dark state back to the bright state, we can repeatedly test a dark-state event to confirm the measurement similar to the approach reported in [**27**].

To measure λ, we first optically pump using 350, 622, and 646 nm lasers until the ion is bright. For this step, we set the threshold count rate to a high value to ensure the initial state is bright with high probability. We then switch off the re-pump lasers and monitor the time the ion remains fluorescent. The distribution of bright times is given in Figure 4.3, which gives a fitted value of $\lambda = 0.624(5)$. Using measured count rates for the bright and dark states of 6.290(5) and 0.560(3) per millisecond, respectively, together with the measured detection efficiency of 0.00326(2) we infer a ratio $w/W = 3.55(6) \times 10^{-7}$. We used an artificial background to match the photon count rate of a bright ion to determine the contribution of the measured rate from detection errors. Out of 1×10^5 events we obtained an average detection time of 6 ms with no errors found. This bounds the contribution to < 0.0016/s, which is well below the statistical uncertainty.

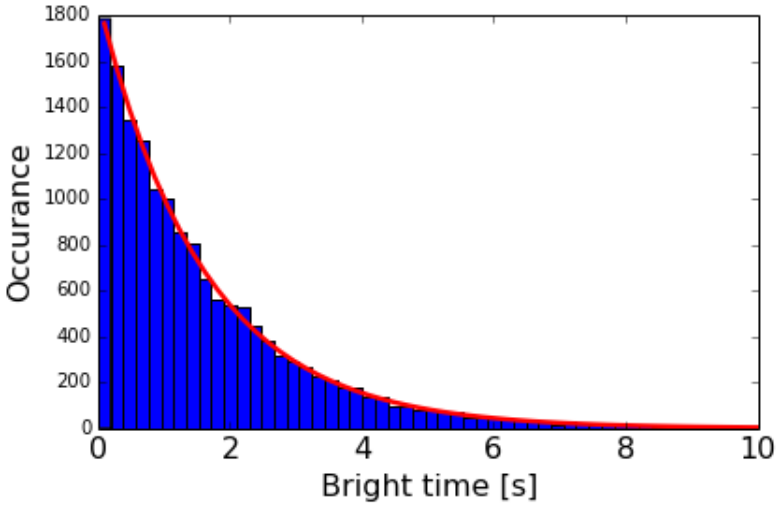

FIGURE 4.3. Histogram of bright times when fluorescing on the $^3D_1$ to $^3P_0^o$ transition.

Decay out of the detection channel is dominated by decays from $^3P_0^o$ to $^1S_0$ and $^3D_2$. In two separate experiments, we determine the contribution from each of these decays by re-pumping using either the 350 or the 622 nm laser after the ion is confirmed dark and measure the fraction returning to the bright state. From these measurements and the branching ratios measured in 2 the percentage of decays going to $^1S_0$ and $^3D_2$ are 0.497(19) and 0.562(30), respectively. These values are in reasonable agreement with theoretical values given in [**1**].

CHAPTER 5

The clock transition

Initial attempts to drive the clock transition were unsuccessful and required two major changes to the experimental set up. Firstly, a new trap was needed to provide tighter confinement of the ion. This was to ensure that motional coupling did not significantly reduce the fidelity at which the clock transition could be driven [**9**]. Secondly, a better clock laser was needed. For this a high performance cavity from Stable Lasers was purchased, which was specified to provide a stability of 10^{-15} at 1 s. In this chapter, we give details of the new trap and the set up of the clock laser. We also show the first observations of driving the clock transition. This experimental effort was carried out altogether with the manpower of a post-doc and a PhD student. The present author of this thesis was involved in the construction and stabilization of the phase lock laser, the optical setup of the lasers attached to the ion trap and the construction of a similar second ion trap

1. A new ion trap design

The new ion trap provided three key improvements over the previous trap. Firstly, the dimensions were reduced so as to provide tighter confinement of the ion to reduce the effects of thermal motion on the probe coupling. Secondly, the trap electrodes were made of copper-beryllium. This alloy has high electrical conductivity to reduce RF power losses, is non-magnetic to reduce any stray magnetic fields, and has high strength relative to pure copper. Thirdly, the ovens are located such that atom flux reaching the trap could be approximately orthogonal to the ionization lasers so as to eliminate any Doppler broadening and shifts.

Similar to the previous design, the trap consists of four rods centered on the vertices of a 1 mm $\times$ 1 mm square, and the end caps are separated by approximately 2 mm. All electrodes are electro-polished to a diameter of approximately

0.45 mm in diameter. The trap is help between two Macor wafers with gold patterned electrodes to provide vertical DC field for micromotion compensation.

The trap is driven by an approximately 20 MHz RF frequency, which is coupled to the trap by a cylindrical helix microwave resonator made of copper. This resonator has a loaded Q-factor of 266. Under typical operating conditions of 7 volts on the end-caps, -1 volts on the DC rods, and an estimated 500 V on the RF electrodes, we measure trap frequencies of (863,771,187) kHz for single $^{138}Ba^{+}$ ion.

Ovens are directed in such a way that 90 degree photo-ionization access is possible. The distance of the oven from the trap is about 46 mm. So for a 1 mm interaction region then we can expect a residual Doppler broadening of around 10 MHz. Barium ovens consist of a thin walled stainless steel tube that is loaded with Barium metal. The lutetium oven consists of a 100 μm thick, 1 mm wide metal foil. Current is fed to each oven via a 0.5 mm diameter tantalum wire that is spot welded to each end of the oven.

2. Clock Laser

In order to provide a highly stable laser for driving the anticipated narrow clock transition we required a stable reference cavity to lock to. A cavity was purchased from Stable Lasers in Boulder, Colorado. The cavity is a high finesse cavity using a 10 cm ultra-low expansion (ULE) glass spacer, with mirrors from Advanced thin films optically bonded at each end. The cavity has a measured finesse of approximately 4×10^5 giving a measured line-width of 7.5 kHz. Small Viton balls on top of a Zerodur base supports the cavity spacer and the whole construction sits inside a thermal stabilized, heat-shielded vacuum. Placement of the Viton balls minimizes length variation due to vibration. Over the period of a few weeks, the temperature of the system was slowly increased to find the optimum operating point at which the temperature expansion coefficient of the ULE is approximately zero. At this operating point residual cavity drift resulting from 'creep' of ULE has been recently measured to be approximately 150 mHz/s and is slowly diminishing with time. The cavity is specified to have a stability of 10^{-15} in 1 s but we currently have no means to characterize this.

To lock a diode laser to the cavity requires a high bandwidth lock. Although we have successfully locked the laser directly to the cavity it was prone to lose lock throughout the day when subject to external noise as encountered in lab. To fix this, a more passively stable laser design was used along with pre-stabilization to a medium finesse cavity. In addition, 3 clock lasers in total will be needed for full operation. One approach would be to lock three independent lasers to the cavity, but in this work we successfully demonstrated a direct phase lock between lasers that will ultimately simplify the set-up.

The master laser design is an ECDL but uses an interference filter to frequency select the feedback instead of the usual diffraction grating [**28**]. The filter allows a linear construction, which is less sensitive to vibration. The laser is stabilized in two steps. It is first locked to a 10000-finesse cavity using the usual PDH lock. This is achieved using a 3 MHz servo bandwidth to control the injection current of diode. For long-term drifts, an outer servo loop keeps the DC current control near zero via feedback to a piezoelectric transducer, which adjusts the length of the laser's external cavity. The pre-stabilized laser light is subsequently locked to a high finesse cavity using a slower servo action with an acousto-optic modulator. Both cavity locks use a wideband EOM ($\times$10 GHz bandwidth), to provide a tunable offset from the respective cavity.

To be able to drive the other hyperfine levels, two additional lasers are needed. Since the hyperfine splitting for Lu^+ is $\sim$ 10 GHz, we are able to use a phase lock to provide the additional lasers. Quite simply, light from both the master laser and a second laser are beat together on a fast photo-diode and the beat-note is locked to an appropriate microwave oscillator signal. Light from each stabilized laser passes through an AOM and is then used to injection lock a slave laser. The AOM provides the ability to switch between frequencies associate with either side of a resonance, and to different Zeeman sublevels. For $^{175}Lu^+$, the Zeeman states can be separated by a few MHz. The slave laser configuration conveniently eliminates power variations with frequency and boosts the clock power. With $^{176}Lu^+$ the additional slaves will likely not be needed. The entire clock laser set up is shown schematically in Fig. 5.1.

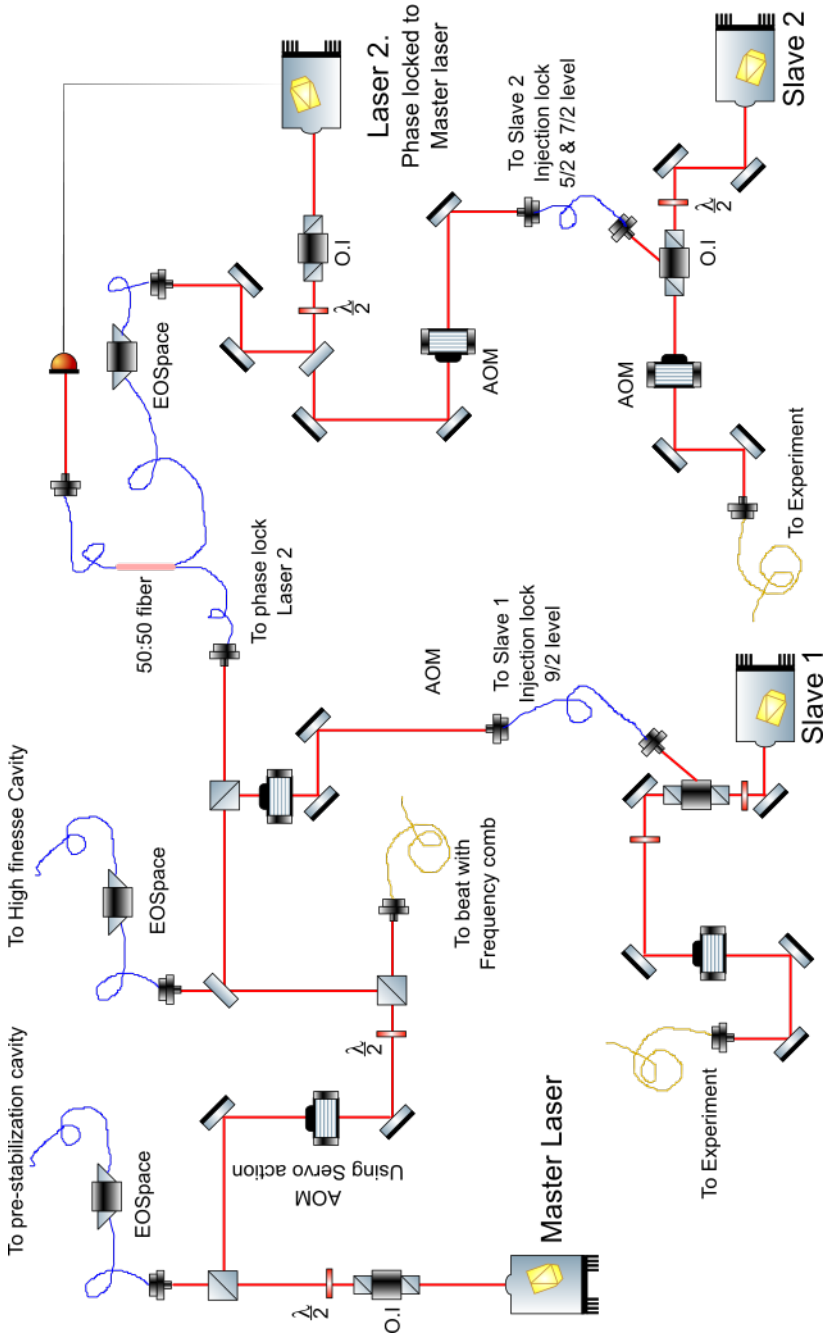

FIGURE 5.1. Optical diagram for the clock laser.

3. First observation of the clock transition

Driving the clock transition first entails the arduous task of finding the right frequency of the transition. Available power of the diode lasers gave an estimated power broadened linewidth around 1 kHz, and the transition was only known to

within several MHz at best. For an initial estimate, we used a technique from a previous Masters thesis. The atom was pumped into the $^1S_0$ and the clock laser was continuously swept across a particular frequency range with the 646 nm detection laser always on. Broadening from the 646 nm light provides quantum jumps over a frequency range of several MHz giving a smaller frequency range over which to search for the transition.

Once the search region is determined, the atom is first pumped into the $\left|^3D_1, F = 9/2, m_F = +9/2\right\rangle$ state. This is done with an optical pumping beam propagating at an angle of about 30° relative to the quantization axis, with the polarization adjusted so as to give only σ^+ and π components. A clock laser pulse of several milliseconds is then followed by detection. The clock laser propagates transverse to the trap and has the polarization along the quantization axis, which is also transverse to the trap. This configuration minimizes motional coupling and allows $\Delta m = \pm 1$ transitions to be driven. This ultimately provided the first observation of the clock transition as illustrated in Fig. 5.2.

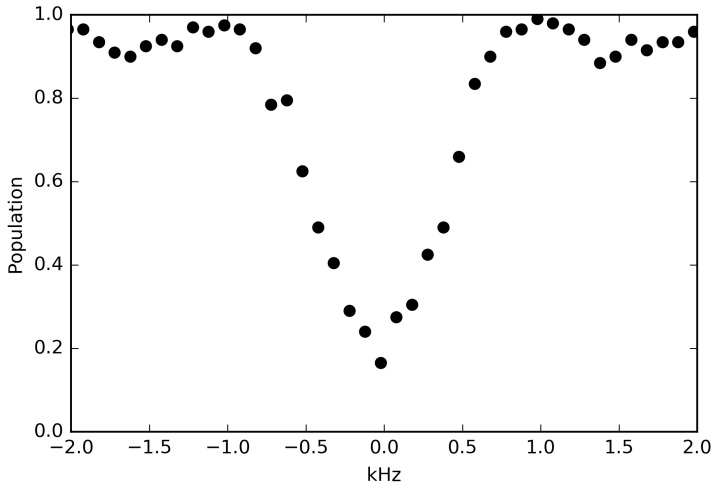

FIGURE 5.2. Frequency scan over the line $\left|^3D_1, F = 9/2, m_F = +9/2\right\rangle$ to $\left|^1S_0, F = 7/2, m_F = +7/2\right\rangle$.

With the clock transition established, we were then able to demonstrate the driving of the other hyperfine state. With two clock lasers overlapped, we first drive $\left|^3D_1, F = 9/2, m_F = +9/2\right\rangle$ to $\left|^1S_0, F = 7/2, m_F = +7/2\right\rangle$ and then detect

to verify the atom has been prepared in the ground state. If so we then drive $\left|{}^1S_0, F = 7/2, m_F = +7/2\right\rangle$ to $\left|{}^3D_1, F = 7/2, m_F = +5/2\right\rangle$. This transition is much less sensitive to magnetic fields owing to the much smaller Lande g-factor and smaller m_F for the upper state allowing the transition to be more cleanly driven. The transition, and Rabi flopping for this transition is shown in Fig 5.3.

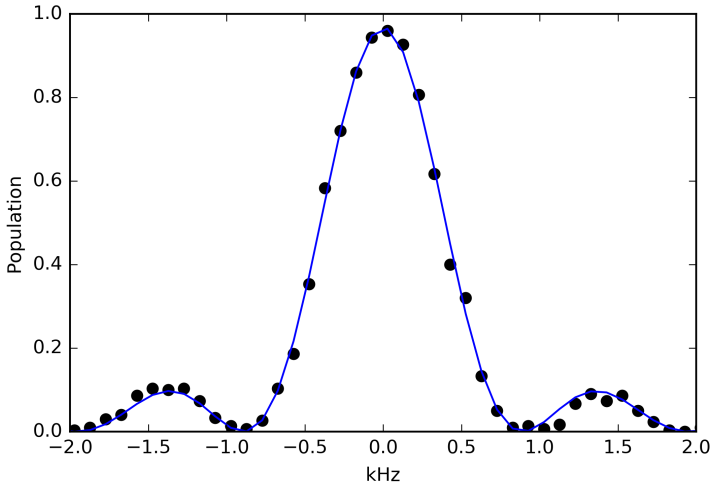

(a)

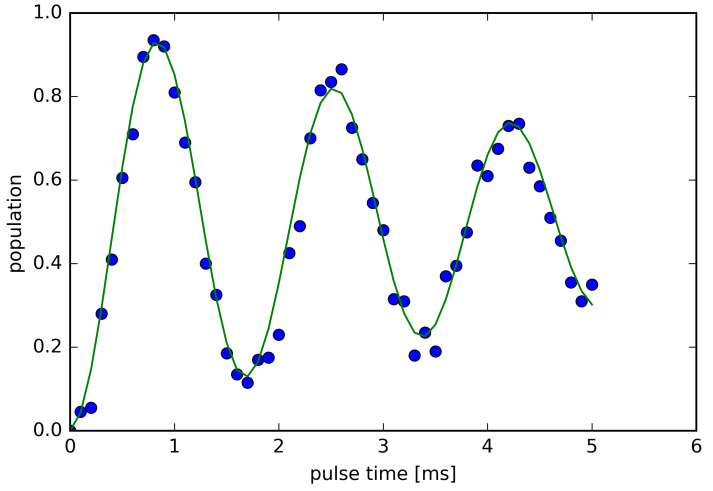

(b)

FIGURE 5.3. (a) Frequency scan and (b) Rabi flop over the line $\left|{}^1S_0, F = 7/2, m_F = +7/2\right\rangle$ to $\left|{}^3D_1, F = 7/2, m_F = +5/2\right\rangle$.

The results here constitute the first observation of the $^1S_0$ to $^3D_1$ clock transition. They provide the necessary apparatus to demonstrate clock operation and to measure the hyperfine structure of the $^3D_1$ level. They also establish the major components needed for full clock operation, which involves averaging over multiple hyperfine states.

CHAPTER 6

Conclusion

In this work we have taken the first steps in establishing an operational optical atomic clock using singly ionized Lu^+. This has involved the set up of a laser system to provide detection, optical pumping and state preparation. Using this system, together with an existing linear Paul trap, has allowed us to make a measurements of branching ratios from $^3P_1$ level used for optical pumping, and lifetime measurements of the $^1D_2$ and $^3D_2$ clock states. In addition we have measured small branching ratios associated with highly forbidden decays out of the $^3P_0$ level. These measurements have allowed a first comparison to atomic structure calculations.

In a new trap we have also established the first observation of the $^1S_0$ to $^3D_1$ clock transition. The coupling strength inferred from this observation has allowed us to estimate the lifetime of the $^3D_1$ level giving a value of approx. 90 hours. This works establishes all the major components needed to implement clock operation over all three hyperfine states allowing a systematic study clock properties such as the hyperfine splitting, and the differential scalar polarizability $\Delta\alpha_0$.

In this work, we have used $^{138}Ba^+$ for sympathetic cooling. This has been done for technical reasons associated with decay into the $^1D_2$ level at which point Lu^+ becomes optically inactive for typically a fraction of a second. This can be easy fixed using an additional laser at 895nm and such a laser has already been put in place during the write up of this thesis. Our work has used only the $^{175}Lu^+$ isotope due to limitations imposed by the oven geometry. Improvements in the new trap have allowed the first loading of $^{176}Lu^+$ although spectroscopy of the relevant transitions is still needed before clock operation can be established with this ion.

An important next step is to measure the DC scalar polarizability of the $^1S_0$ to $^3D_1$ to resolve the current ambiguity between two independent atomic structure calculations. Should the polarizability prove to be negative, the $^1S_0$ to $^3D_1$ transition would provide the opportunity to explore the possible of a many-ion clock as proposed in [**16**]. If not, the $^1S_0$ to $^3D_2$ transition may be used instead, albeit with a more sophisticated clock operation. Measurements are currently under way to determine the future prospects of the new clock candidate.

Bibliography

[1] Eduardo Paez, KJ Arnold, Elnur Hajiyev, SG Porsev, VA Dzuba, UI Safronova, MS Safronova, and MD Barrett. Atomic properties of lu+. *Physical Review A*, 93(4):042112, 2016. ix, 11, 13, 31, 32, 34, 35, 37

[2] Serge Haroche. Nobel lecture: Controlling photons in a box and exploring the quantum to classical boundary. *Reviews of Modern Physics*, 85(3):1083, 2013. 1

[3] Francesco Scazza, Christian Hofrichter, Moritz Höfer, PC De Groot, Immanuel Bloch, and Simon Fölling. Observation of two-orbital spin-exchange interactions with ultracold su (n)-symmetric fermions. *Nature Physics*, 10(10):779–784, 2014. 1

[4] N Huntemann, B Lipphardt, Chr Tamm, V Gerginov, S Weyers, and E Peik. Improved limit on a temporal variation of m p/m e from comparisons of yb+ and cs atomic clocks. *Physical review letters*, 113(21):210802, 2014. 1, 9

[5] T Kessler, C Hagemann, C Grebing, T Legero, U Sterr, F Riehle, MJ Martin, L Chen, and J Ye. A sub-40-mhz-linewidth laser based on a silicon single-crystal optical cavity. *Nature Photonics*, 6(10):687–692, 2012. 1

[6] Andrew D Ludlow, Martin M Boyd, Jun Ye, Ekkehard Peik, and Piet O Schmidt. Optical atomic clocks. *Reviews of Modern Physics*, 87(2):637, 2015. 3

[7] WM Itano, JC Bergquist, JJ Bollinger, JM Gilligan, DJ Heinzen, FL Moore, MG Raizen, and DJ Wineland. Quantum projection noise: Population fluctuations in two-level systems. *Physical Review A*, 47(5):3554, 1993. 4, 5

[8] Norman F Ramsey. Experiments with separated oscillatory fields and hydrogen masers. *Reviews of modern physics*, 62(3):541, 1990. 4

[9] David J Wineland, C Monroe, Wayne M Itano, Dietrich Leibfried, Brian E King, and Dawn M Meekhof. Experimental issues in coherent quantum-state manipulation of trapped atomic ions. *arXiv preprint quant-ph/9710025*, 1997. 4, 39

[10] Masao Takamoto, Feng-Lei Hong, Ryoichi Higashi, and Hidetoshi Katori. An optical lattice clock. *Nature*, 435(7040):321–324, 2005. 4

[11] BJ Bloom, TL Nicholson, JR Williams, SL Campbell, M Bishof, X Zhang, W Zhang, SL Bromley, and J Ye. An optical lattice clock with accuracy and stability at the 10-18 level. *Nature*, 506(7486):71–75, 2014. 5

[12] N Hinkley, JA Sherman, NB Phillips, M Schioppo, ND Lemke, K Beloy, M Pizzocaro, CW Oates, and AD Ludlow. An atomic clock with 10–18 instability. *Science*, 341(6151):1215–1218, 2013. 5

[13] TL Nicholson, SL Campbell, RB Hutson, GE Marti, BJ Bloom, RL McNally, W Zhang, MD Barrett, MS Safronova, GF Strouse, et al. Systematic evaluation of an atomic clock at 2 [times] 10-18 total uncertainty. *Nature communications*, 6, 2015. 5

[14] DJ Berkeland, JD Miller, JC Bergquist, WM Itano, and DJ Wineland. Minimization of ion micromotion in a paul trap. *Journal of Applied Physics*, 83(10):5025–5033, 1998. 6, 12

[15] MD Barrett. Developing a field independent frequency reference. *New Journal of Physics*, 17(5):053024, 2015. 6, 7, 9

[16] Kyle Arnold, Elnur Hajiyev, Eduardo Paez, Chern Hui Lee, MD Barrett, and John Bollinger. Prospects for atomic clocks based on large ion crystals. *Physical Review A*, 92(3):032108, 2015. 6, 7, 12, 48

[17] Pierre Dubé, Alan A Madej, Zichao Zhou, and John E Bernard. Evaluation of systematic shifts of the 88 sr+ single-ion optical frequency standard at the 10^{-17} level. *Physical Review A*, 87(2):023806, 2013. 7, 12

[18] WM Itano, JC Bergquist, A Brusch, SA Diddams, TM Fortier, TP Heavner, L Hollberg, DB Hume, SR Jefferts, L Lorini, et al. Optical frequency standards based on mercury and aluminum ions. In *Optical Engineering+ Applications*, pages 667303–667303. International Society for Optics and Photonics, 2007. 9

[19] Nils Huntemann, M Okhapkin, B Lipphardt, S Weyers, Chr Tamm, and E Peik. High-accuracy optical clock based on the octupole transition in yb+ 171. *Physical Review Letters*, 108(9):090801, 2012. 9

[20] MD Barrett. Developing a field independent frequency reference. *New Journal of Physics*, 17(5):053024, 2015. 9

[21] Alexander Kozlov, VA Dzuba, and VV Flambaum. Optical atomic clocks with suppressed blackbody-radiation shift. *Physical Review A*, 90(4):042505, 2014. 11

[22] CHUAH BOON LENG. *ION TRAP CAVITY QUANTUM ELECTRODYNAMICS*. PhD thesis, Centre for Quanutm Technologies, 2013. 15

[23] GOH Wei Na. Photoionization of neutral barium. Master's thesis, Centre for Quantum Technologies, 2011. 17

[24] Nicholas C. Lewty. *EXPERIMENTAL DETERMINATION OF THE NUCLEAR MAGNETIC OCTUPOLE MOMENT OF 137Ba*. PhD thesis, Centre for Quantum Technologies, 2013. 17, 18

[25] Arifin. Lutetium ion spectroscopy. Master's thesis, Centre for Quantum Technologies, 2014. 18

[26] Boon Leng Chuah, Nicholas C Lewty, and Murray D Barrett. State detection using coherent raman repumping and two-color raman transfers. *Physical Review A*, 84(1):013411, 2011. 25

[27] AH Myerson, DJ Szwer, SC Webster, DTC Allcock, MJ Curtis, G Imreh, JA Sherman, DN Stacey, AM Steane, and DM Lucas. High-fidelity readout of trapped-ion qubits. *Physical Review Letters*, 100(20):200502, 2008. 30, 36

[28] X Baillard, A Gauguet, S Bize, P Lemonde, Ph Laurent, A Clairon, and P Rosenbusch. Interference-filter-stabilized external-cavity diode lasers. *Optics Communications*, 266(2):609–613, 2006. 41